

Comparison of 3D MT inversions for geothermal exploration: Case studies for Krafla and Hengill geothermal systems in Iceland



Gudni Karl Rosenkjaer^{a,c,*}, Erika Gasperikova^b, Gregory A. Newman^b, Knutur Arnason^c, Nathaniel J. Lindsey^b

^a University of British Columbia, 6339 Stores Road, Vancouver, BC V6T 1Z4, Canada

^b Lawrence Berkeley National Laboratory, 1 Cyclotron Road, MS74R316C, Berkeley, CA 94720, United States

^c Iceland Geosurvey, Grensasvegur 9, 108 Reykjavik, Iceland

ARTICLE INFO

Article history:

Received 25 November 2014

Accepted 2 June 2015

Available online 23 July 2015

Keywords:

Magnetotellurics

3D inversion

Geothermal

Iceland

Krafla

Hengill

ABSTRACT

The magnetotelluric (MT) method is important for exploration of geothermal systems. The information on the Earth's resistivity obtained with MT methods has been valuable in imaging the hydrothermal alteration of such systems. Given its ability to recover complex resistivity models for the Earth, three-dimensional (3D) MT inversion has become a common practice in geothermal exploration. However, 3D inversion is a time-consuming and complicated procedure that relies on computer algorithms to search for a model that can explain the measured data to a sufficient level. Furthermore, many elements of inversion require input from the practitioner, which can easily bias the results. Consequently, final 3D MT results depend on various factors, including the inversion code, the model mesh used to represent the Earth, data quality and processing, and constraints imposed during the inversion procedure.

In this paper, to explore how this variability in 3D MT modeling impacts the final model, we invert MT data sets from the Krafla and Hengill geothermal areas in Iceland, using three different inversion codes. In each case, the modelers had the freedom to select a subset of the data and implement the inversion for the respective code in an optimized way. We compare the results from all the inversion codes, as well as consider the setup and assumptions made during the inversion process, all of which helps enhance the robustness and quality of the results. The comparison is done in multiple ways, using visual comparison of the recovered resistivity models, as well as comparing the structural similarities of the models by employing a structural correlation metric based on cross-gradients and other types of metrics for structural correlation. This approach highlights structures that are common in all three models, and implies that these structures are independent of the inversion code and necessary to fit the data.

All modeling results from both Krafla and Hengill are consistent to first order, recovering a conductive layer on top of a resistive core typical of high temperature geothermal systems. For Hengill, the models show strong structural agreement, with all inversions recovering a moderately layered resistivity model but adding detail to previous work done in the area. Major differences are found in areas with coarse data coverage and hence questionable model resolution. Where the recovered structures in different models coincide, our confidence that these structures are well-constrained by the data is elevated, in spite of the different setup and assumptions in the codes these structures are required; so they can be interpreted in terms of geology with more certainty. Results from Krafla are not as consistent as results for Hengill, related in part to the Krafla data being noisier than the Hengill data. The models from Krafla have coinciding larger structures, but small-scale structures there are less coherent. One of the consistent structures in all the models is a conductive zone reaching from a depth of 5 km to shallower depths in the northern part of the area.

© 2015 Elsevier Ltd. All rights reserved.

1. Introduction

To investigate the subsurface using magnetotelluric (MT) measurements, we use 3D inversion, which has become standard practice in geothermal exploration. MT technology enables detailed

* Corresponding author at: University of British Columbia, 6339 Stores Road, Vancouver, BC V6T 1Z4, Canada. Tel.: +1 7788482324.

E-mail address: grosenkj@eos.ubc.ca (G.K. Rosenkjaer).

imaging of the geological structures and hydrothermal alteration zones that characterize the geothermal system ([Árnason et al., 2010](#); [Heise et al., 2008](#); [Newman et al., 2008](#)).

Development of 3D MT inversion codes in the last decade has led to greater use of 3D inversion for MT surveying. These codes formulate the inverse problem in different ways, taking advantage of differing numerical algorithms to increase accuracy and accelerate the process. There has been considerable effort put into researching the strengths and weaknesses of different inversion approaches. [Miensopust et al. \(2013\)](#) reviews conclusions of two workshops hosted by the Dublin Institute for Advanced Studies, wherein both code developers and practitioners/modelers from academia and industry came together to assess the status of 3D modeling and inversion of MT data. MT responses were calculated by the participants using the same resistivity model, and responses were compared. As for inversion of MT data, synthetic data produced for mystery models were inverted by the participants. An important finding was that most codes have reasonable qualitative agreement, but differences arise from how the inversion codes were set up and used. Some of the factors that led to differences are pre-processing of the data; selection of stations, components, and/or frequencies used for the inversion; assessment and error assignment for the desired level of misfit; model discretization; and setup of the inversion constraints.

Geothermal systems pose additional challenges for 3D MT inversion. Geothermal systems are structurally complex, often associated with volcanic complexes having significant topographic relief and inhomogeneous materials. While the resistivity of geothermal systems is influenced by multiple petrophysical and geological processes that have occurred in the system, hydrothermal alteration, temperature, and conduction mechanisms are considered to be the major influences ([Flóvenz et al., 2012](#)).

The goal of this work is to compare results from two geothermal fields in Iceland, Krafla and Hengill, using three different 3D MT inversion codes to recover the resistivity structures of these fields. The codes used in this paper are the MT3DInv ([Farquharson et al., 2002](#)), EMGeo ([Newman and Alumbaugh, 2000](#)) and WSINV3DMT ([Sripunvaraporn et al., 2005](#)). In order to better assess the robustness of running an inversion on real data sets, the only restriction imposed is that all the data used for the inversions be from the same pre-processed MT dataset. Otherwise, the modeler had full control over how the inversion was designed (including selecting a subset from the data set), both in terms of stations and frequencies, and in assessing and assigning appropriate measurement uncertainties. To achieve a better control in comparing structures in the models, we calculated gradients and Laplacians of the logarithmic transforms for the resulting resistivity models (in addition to discussing the resulting models). We also employed cross-gradients to map the structural similarities and dissimilarities between the respective models.

2. Magnetotelluric method

The MT method is a passive electromagnetic (EM) method, in which the source fields are a wide spectrum of EM waves that naturally occur due to lightning discharges and interactions between the solar wind and the Earth's magnetosphere ([Cagniard, 1953](#)). The source-wave fields are considered to be arbitrarily polarized plane waves that propagate vertically into the Earth since refraction of EM waves at the interface of air and Earth is high. The depth of investigation (δ_{MT}) can be estimated from the skin depth rule:

$$\delta_{MT}(f) = \sqrt{\frac{\rho}{\mu\pi f}} \approx 500\sqrt{\frac{\rho}{f}} \text{ in [m].} \quad (1)$$

Here δ_{MT} is an estimate of the depth at which the source wave amplitude has attenuated to e^{-1} from its surface value for a given frequency (f) and an estimated resistivity (ρ) of the subsurface. By measuring orthogonal electric (E) and magnetic (H) fields at the surface one can retrieve information about the subsurface resistivity structure, from a few meters to hundreds of kilometers depth. The orthogonal horizontal components of the E and H fields (E_x, E_y, H_x, H_y) are interrelated by

$$\begin{bmatrix} E_x \\ E_y \end{bmatrix} = \begin{bmatrix} Z_{xx} & Z_{xy} \\ Z_{yx} & Z_{yy} \end{bmatrix} \begin{bmatrix} H_x \\ H_y \end{bmatrix}, \quad (2)$$

where the surface impedance (Z) is a 2×2 complex tensor. During recording, Z is calculated for each MT station as a function of frequency. By taking the ratio of the fields measured at the same time, the source effects of the MT fields cancel; therefore, Z can be used to deduce the electrical properties of the Earth, without the need for a more complete description of the MT source field effects (i.e., vertically incident plane wave excitation will suffice). Impedance data are often presented as apparent resistivity and phase

$$\rho_{ij}^{app}(f) = \frac{1}{2\pi\mu_0 f} |Z_{ij}(f)|^2 \text{ and}$$

$$\phi_{ij}^{app}(f) = \arctan \left(\frac{Im(Z_{ij}(f))}{Re(Z_{ij}(f))} \right) \text{ where } i, j = \{x, y\} \quad (3)$$

in order to provide more intuitive values to inspect and interpret the MT response ([Vozoff, 1991](#)). In this paper, as commonly done in geothermal exploration, only the off-diagonal elements are used for the analysis. Using the full impedance tensor has been shown to improve recovery of deep structures (e.g., [Kiyani et al., 2013](#)) and should be considered in future work. However, using the full tensor demands more computational power in solving the inverse problem, particularly for inverse algorithms based upon a data space implementation, and requires an accurate and delicate assessment of error weights with respect to the data objective function. If that requirement is not fulfilled, the inversion results may not be geologically meaningful, compared to those obtained by exclusively using off-diagonal elements. Moreover, for most of the data considered in this study, the on-diagonal elements of the impedance tensor are an order of magnitude smaller than the off-diagonal elements, suggesting that most of the information is contained in the off-diagonal elements. Test inversions were performed using the full impedance and off-diagonal tensor data to assess the contribution of the on-diagonal data. These tests revealed similar resistivity structures in both cases, supporting the notion that the resistivity can be resolved essentially from off-diagonal tensor data.

Galvanic distortion, commonly referred to as static shift, is caused by near-surface inhomogeneous resistivity distributions as well as topography and can create static (amplitude) shifts in MT soundings. The static shift can be addressed using TEM data as described in [Árnason et al. \(2010\)](#). [Stark et al. \(2013\)](#) shows how including a detailed elevation model in a forward modeling of a halfspace produces considerable static shift and suggest that large part of distortion can be explained by topographic affect alone. Therefore, whereas including detailed topographic information into the model is beneficial, in practice it can be an expensive and cumbersome procedure with a large number of cells needed to capture the details of the topography. At both Krafla and Hengill, auxiliary TEM data sets have been measured in close proximity to the MT soundings, enabling a static shift correction. These TEM data have been used to correct MT data for 3D inversions in Hengill ([Árnason et al., 2010](#); [Rosenkjaer, 2011](#)) and for 1D inversion in Krafla ([Friðleifsson et al., 2014](#)). [Rosenkjaer \(2011\)](#) discusses the use of TEM-static-shift-corrected data, both for a synthetic geothermal system with near surface resistivity inhomogeneities and for MT

data from the Hengill area. Rosenkjaer shows that the static shift correction with TEM data recovers a moderately more agreeable resistivity model in both cases compared to the inversions without the static shift correction. One of the inversion codes used in this study (WSINV3DMT) does not allow for topography to be included in the inversion procedure. Considering all of these factors, we decided to use the TEM static-shift-corrected data for all the inversions, even though two of the inversion codes will explicitly consider topographic variations.

2.1. Krafla MT data

The Krafla geothermal area is located in the Northern Volcanic Zone in Iceland. The area is in an active rift zone with a dominant SSW-NNE fault and fissure direction, crosscut by a WNW-ESE-oriented transform graben (Hjartardóttir et al., 2012). For more detailed discussion of the geology, see Gasperikova et al. (2015).

Fig. 1 shows the topographic relief and locations of MT soundings. In total, 167 MT soundings were collected at Krafla. These MT data were collected in three major field campaigns: by a group from Duke University during the summers of 2004 and 2005 (108 soundings); by Moscow State University, and Iceland Geosurvey in the summers of 2006 (55 soundings); and 2008 (5 soundings). All soundings were collected with equipment from Phoenix Geophysics Ltd., and processed using the software package provided with the instruments. The data-processing package includes the Gamble et al. (1979) remote reference routine. The subsets of the Krafla MT dataset used for individual inversion codes described in Sections 3.1–3.3 are shown in Fig. 1 as red diamonds, green stars, and yellow crosses, respectively.

Fig. 2 shows an example of an MT sounding at Krafla. The responses at frequencies above approximately 10 Hz exhibit a 1D character, where the off-diagonal soundings Zxy and Zyx are parallel and equal in amplitude. The diagonal elements Zxx and Zyy

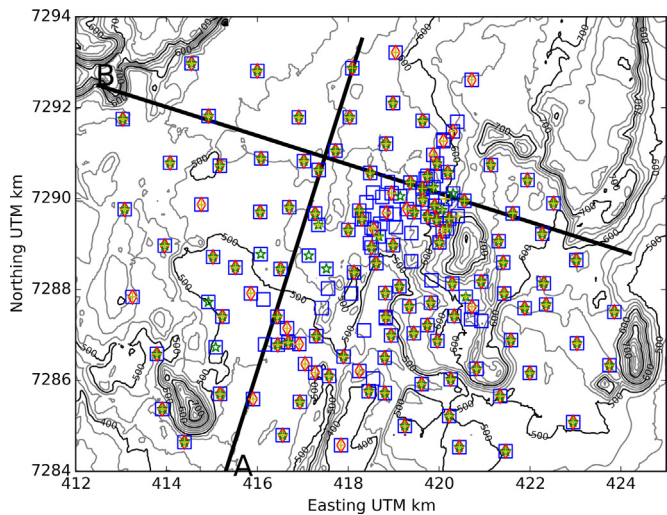


Fig. 1. Topographic map and MT station locations at Krafla. All MT station locations are shown as blue squares. Stations used with WSINV3DMT are shown by red diamonds; stations used with EMGeo are shown as green stars; stations used with MT3DInv are shown as yellow crosses. Black lines (A, B) show sections used for discussion of recovered models in Section 5. (For interpretation of the references to color in this text, the reader is referred to the web version of the article.)

(the green and yellow impedance curves, respectively) are considerably lower in amplitude than the off-diagonal elements for most frequencies. Our assessment of the quality of the Krafla dataset is that it contains a considerable amount of noisy data, increasing the complexity of the inversion process.

2.2. Hengill MT data

The Hengill geothermal area is located in SW Iceland, at the triple junction of the Reykjanes Peninsula, the Western Volcanic

Station at 417896 Easting, 7286525 Northing.

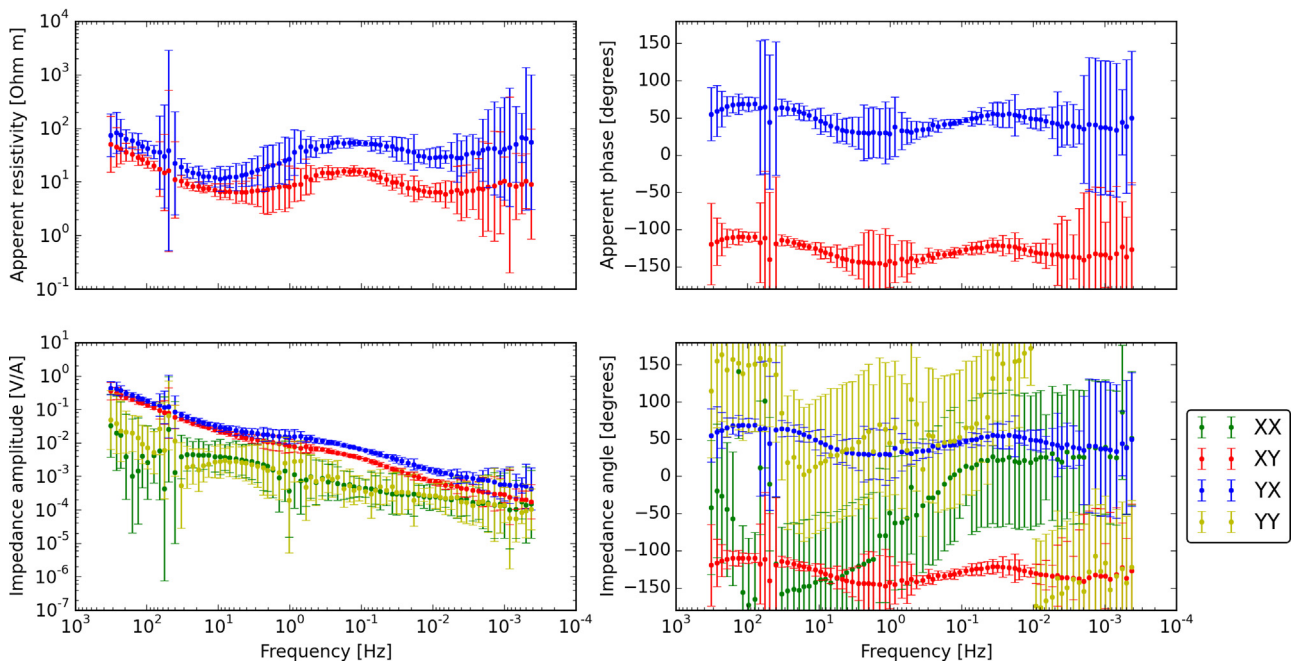


Fig. 2. An example of MT data at Krafla. At the highest frequencies, parallel apparent resistivity and phase curves of Zxy and Zyx components are conspicuous indicating that Earth resistivity is more or less one dimensional in the upper part of the geological section. This finding is also confirmed with the on-diagonal impedance elements, which are significantly smaller in amplitude (at least an order of magnitude) until reaching a frequency of 0.1 Hz. The frequencies are plotted decreasing from left to right. (For interpretation of the references to color in this text, the reader is referred to the web version of the article.)

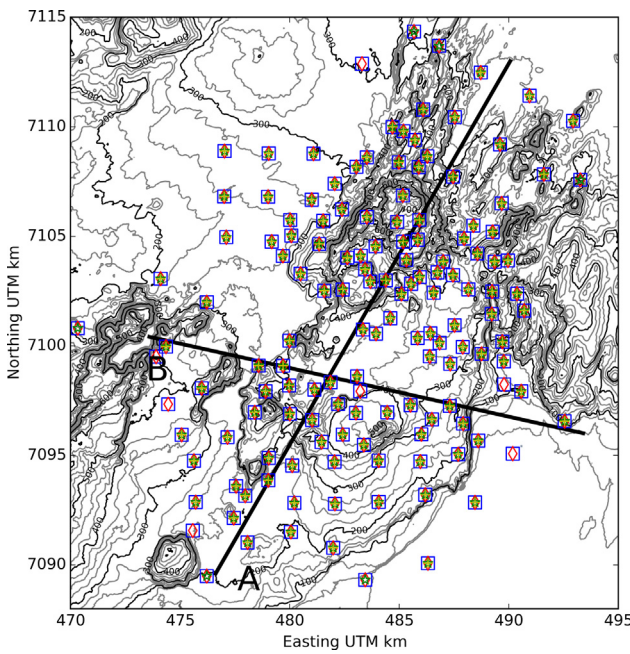


Fig. 3. Topographic map and MT station locations at Hengill. All MT station locations are shown as blue squares. The locations used with WSINV3DMT are shown by red diamonds, locations used with EMGeo are show as green stars, and locations used with MT3DInv are shown as yellow crosses. Black lines (A, B) show sections used for discussion of recovered models in Section 5. (For interpretation of the references to color in this text, the reader is referred to the web version of the article.)

Zone, and the South Iceland Seismic Zone. The active fissure swarm in the area has a SW-NE orientation, coincident with the main volcanic fissure that cuts through the Hengill volcano. Again, for a more detailed discussion of the geology, see Gasperikova et al. (2015).

Fig. 3 shows the topographic relief and locations of MT soundings at Hengill. The original MT data were acquired by the Iceland

Geosurvey in four collection campaigns (Árnason et al., 2010); for this study, a total of 144 soundings were available for the inversion, shown as blue squares in Fig. 3. All the soundings were collected with equipment from Phoenix Geophysics Ltd. In some cases, only the electric fields were collected, and the magnetic field data at a nearby site were used for estimating the impedance tensor. The data were processed with software provided with the instruments, which included a remote reference processing routine (Gamble et al., 1979). Overall, data quality is very good, better than the Krafla dataset. One example of the impedance and apparent resistivity curves are shown in Fig. 4. This example highlights how, like the Krafla example, the off-diagonal elements Zxy and Zyx are equal in amplitude for frequencies above 10 Hz. The diagonal elements Zxx and Zyy are found to be considerably lower in amplitude than the off-diagonal elements for most frequencies.

3. Inversion algorithms

The goal of MT inversion is to construct a resistivity model that produces responses that fit the observed data within a given tolerance. Owing to the non-uniqueness of the 3D MT inversion problem, we must regularize the procedure by enforcing constraints on an acceptable model. This is commonly done by requiring the model to change gradually between adjacent cells: by using a reference model to enforce a priori information; and/or by restricting the range of resistivity values that can be used in the inverse solution. The choice and implementation of the constraints will influence the recovered model, which also needs to be designed considering prior knowledge of the problem and the geological settings at any given place. The inversion problem can be described with the generalized objective function

$$\phi = \phi_d + \beta\phi_m, \quad (4)$$

where ϕ is the overall objective function, ϕ_d is a data misfit measuring the difference between the predicted and observed data, ϕ_m is the model misfit introducing constraints to the model, and β is

Station at 484065 Easting, 7094764 Northing.

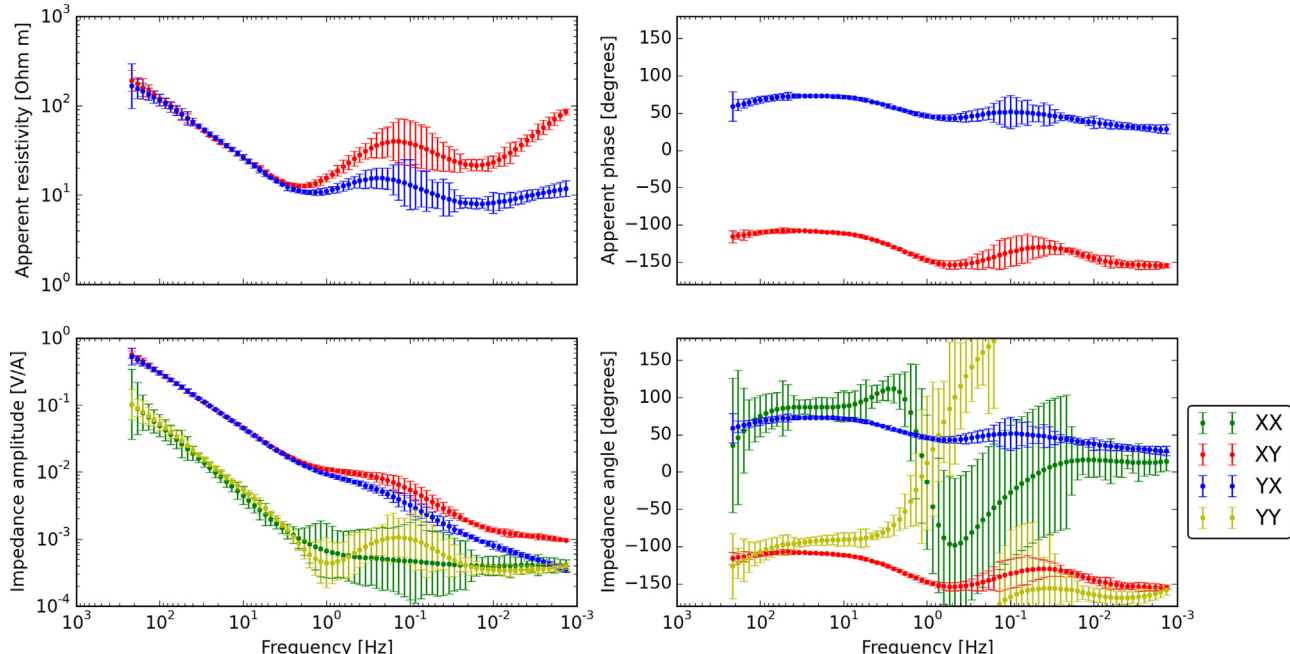


Fig. 4. An example of MT data from Hengill. The data show a 1D character at the highest frequencies, above 10 Hz in the Zxy and Zyx components. Additionally, the on-diagonal impedance elements are significantly smaller in amplitude (an order of magnitude) for most of the frequency range.

the trade-off parameter controlling relative significance between the data and model misfits in the overall objective function. Estimating an appropriate value for β is important, because a large β will poorly fit the data, due to the heavy influence of the model constraint introduced in the model misfit term in Eq. (4), whereas a small β will fit the data better by requiring more structure in the recovered model because of the lower importance of the model constraints (Oldenburg and Li, 2005). A common way of estimating trade-off parameters is to use a cooling scheme: the inversion is started with a large β , which then gradually decreases in value as the inversion progresses. The inversion progresses to a new β only after effectively converging for the previous one, when the inversion process for a fixed β is found to be making minimal progress in further reducing the misfit of the objective function. The global goal of the inversion is to fit the data to a pre-specified tolerance, assuming that the estimations of data errors in the data misfit term are valid.

During each iteration step of the inversion, multiple forward calculations of the resistivity model are required. The number of times the forward problem needs to be solved depends on the number of unique frequencies and number of model evaluations required at each inversion iteration step. The complexity of each of these forward solutions will depend on the number of cells in the mesh and the efficiency of the solver algorithm.

Note that 3D MT inversion algorithms can be implemented in different ways; Siripunvaraporn (2011) gives a good overview of common numerical algorithms used in MT. Parallelization of the inversion algorithms is also an important factor in their speed and usability. Distributing the calculations over multiple CPU threads significantly reduces the time required to solve the problem and allows for bigger systems to be solved by increased CPU power and shared memory of the threads, respectively. Running on multiple CPUs significantly improves efficiency, making the solution of larger and more realistic inversion problems feasible.

In this study, we use three different inversion codes to invert data from the Hengill and Krafla geothermal areas in Iceland. These inversion codes are discussed briefly below; more detailed descriptions of these codes can be found in given references.

3.1. WSINV3DMT

The WSINV3DMT inversion code uses a data-space variant of the minimum-structure Occam inversion approach. Following Siripunvaraporn et al. (2005), the objective function to be minimized is

$$U(m, \lambda) = (m - m_0)^T C_m^{-1} (m - m_0) + \lambda \{ (d - F[m])^T C_d^{-1} (d - F[m]) - X^*{}^2 \}, \quad (5)$$

where m and m_0 are the resistivity model and the prior resistivity model, respectively, C_m is the model covariance matrix, which contains information about model regularization, d is observed data, $F[m]$ is forward calculated predicted data, C_d is the data covariance matrix containing information about the data uncertainties, X^* is the desired level of misfit, and λ is the trade-off parameter. A parallelized solution strategy shown in Eq. (5) is described in Siripunvaraporn and Egbert (2009). WSINV3DMT assumes a flat surface in the model discretization; thus, one cannot include topography.

3.2. EMGeo

The EMGeo inversion code uses a nonlinear conjugate-gradient optimization scheme (Newman and Alumbaugh, 2000) with an approximate Hessian as a pre-conditioner (Newman and Boggs, 2004). The objective function is a weighted sum of the data misfit,

and includes a model regularization that allows for smooth model reconstructions along with a reference model. Here, the objective function is given as

$$\varphi = \sum_{n=1}^{2N} \left[\frac{(Z_n^{obs} - Z_n)}{\epsilon_n} \right]^2 + \lambda (m - m_{ref})^T W^T W (m - m_{ref}), \quad (6)$$

where Z_n^{obs} and Z_n are the observed data and predicted data for the n th data, respectively, ϵ_n is the data misfit of the n th data, and W consists of a finite difference approximation of the model Laplacian operator. In Eq. (6), the regularization parameter λ controls model regularization in the objective function. This algorithm has proven successful in previous 3D MT imaging studies of geothermal fields (see Newman et al., 2008).

During the inversion, the regularization parameter λ is decreased; initially a large fixed value is used, which decreases incrementally during the inversion. In other words, as the inversion progresses, the weight of the model regularization decreases in Eq. (6), allowing for rougher structures to be incorporated into the model, as needed. The inversion runs until an appropriate data misfit is achieved. The inversion code is optimized to run on a large number of cores, in which calculations can be distributed and solved simultaneously to reduce the time to solution.

3.3. MT3Dinv

The MT3Dinv inversion code uses an iterative Gauss-Newton procedure to solve the inverse problem (Farquharson et al., 2002). It searches for a minimum of the objective function

$$\phi = \|W_d(F(m) - d^{obs})\|_2^2 + \beta \sum_k (\alpha_k \|W_k(m - m_{ref})\|_2^2) . \quad (7)$$

$$k=s,x,y,z$$

where m is a vector expressing the model parameters, m_{ref} is the reference model, W_d is the diagonal matrix containing the data uncertainties, d^{obs} is the observed data, and $F(m)$ is the forward modeling operator that produces a response for a given resistivity model. β is the trade-off parameter between the data and model misfits, W_s is a diagonal damping matrix, and W_x , W_y , W_z are the first order finite-difference matrices in the x , y , and z directions in the model, respectively. α_s , α_x , α_y and α_z are scaling factors that control the importance of prior model information and constraints in the objective function, described by the model misfit in Eq. (7). Further constraints can be introduced into model, where bounds on the allowed conductivity values can be implemented. This can be done globally for all the cells in the model, where all values are within a conductivity range; or locally for each cell, where each cell has its own conductivity bound.

The regularization parameter β is decreased during the inversion process. Starting with a large value for β , the optimization problem is solved iteratively at each step, until either the appropriate misfit error has been achieved or the maximum number of iterations is reached. Once finished, the model is updated, β is decreased, and the process is repeated until a satisfactory data misfit is reached. An option is implemented in the code to allow for m_{ref} to be updated for each new β using the resulting model from the previous iteration. This can increase the convergence rate of the inversion problem. The code is parallelized to distribute the solution of the MT source fields for each frequency on different compute cores, significantly increasing the speed of the inversion process.

4. Description of inversions

Owing to the non-uniqueness of the inversion procedure, the same data set can be fit to the same degree with different resistivity models. Thus model interpretation is best done in the context of, or

in conjunction with, other available information about a region, e.g., geological information, other geophysical data, and borehole data. Running multiple inversions with different settings and inputs, and using multiple starting models is considered the current best practice. It provides a fair control on which structures and features are required by the data and which are not (and should be considered as artifacts).

It is usually impractical to invert data for all measured frequencies, since computational requirements for the inversion codes are highly dependent on the number of frequencies. Care must be taken to select frequencies that correspond with the desired depth of investigation, and to remove noisy data by either excluding them from the data set or by assigning larger errors. There are, in fact, many important and delicate steps regarding data input that need to be taken in order for an inversion to run effectively. These include understanding the data that are used in the inversion, providing consistent data with regard to the units that the inversion algorithm requires, ensuring that the data vectors align with the coordinate axes used in the algorithm, and ensuring that the assumption of time dependency $e^{-i\omega t}$ or $e^{i\omega t}$ for the data matches that of the algorithm. If these steps are not addressed, the inversion will not be able to function properly and will not converge to a satisfactory solution. [Siripunvaraporn \(2011\)](#) discusses these issues and provides guidelines for addressing them within the inversion process.

Mesh design also plays an important role in the solution of the problem. When discretizing the Earth, the tradeoff between accuracy, which generally requires a large number of cells, and efficiency, which generally requires reducing the computational requirements, needs to be considered. Furthermore, it is important to discretize the Earth such that numerical errors are minimized by using small enough cells, but without exceeding the limits of the memory and CPU power available for solution of the inverse problem.

Another source of numerical errors may arise from the mesh boundaries. It is common to assume 1D or 2D field behavior as boundary conditions. To account for such conditions, the core mesh (the part of a model that contains the data and has uniform horizontal cell sizes) is padded with cells that progressively increase in size away from the core mesh. This minimizes the influence of the boundary conditions in calculations of predicted MT soundings, data sensitivities, and functional gradients.

In practice, running an inversion also requires the user to set parameters that control the weights of the different terms in the objective function, as well as other settings required by numerical solvers and optimization algorithms employed within the inversion code. Having a basic understanding of what these settings are and how they may affect the results is important, to improve the interpretation of the model. It is important to be mindful of the inversion process setup, data quality; discretization and inversion settings. For example, when a coarse mesh and low frequencies are used, detail structures in the near surface cannot be resolved. Similarly, smooth regularization does not allow for sharp interfaces between resistivity units. In the following section, we will discuss the setups of the inversion codes used in this study. The same initial static shift corrected data set was available to the users, but each user selected a subset of the data (both locations and frequencies) and assigned errors as appropriate for the particular code. [Figs. 1 and 3](#) show the MT stations used for Krafla and Hengill, respectively. No restrictions were enforced in terms of the starting model choices, the details of how the inversions were run, or the constraints imposed on the different inversion codes.

4.1. WSINV3DMT

Some of the key parameters used in the WSINV3DMT inversion for the Hengill and Krafla areas are described in [Table 1](#).

The mesh used in the Hengill area is based on a local reference frame that is rotated 30° clockwise from true North. The mesh used for Krafla is on a frame parallel to the UTM grid. Padding cells were added to the sides of the core mesh, where the side padding was incrementally increased in size by a factor ranging from 1.2 to 1.8. The mesh contains 28 cells in the vertical direction, growing by a factor of 1.4 from thickness of 8 m to 65 km at the bottom mesh boundary. In both areas, no topography is incorporated within the model. Data errors used in the covariance matrix were set to the variances provided in the EDI files, but a minimum uncertainty error floor was set at 3% and 5% of a given data value for Hengill and Krafla data, respectively. Each inversion was implemented in stages, with the observed data (frequencies and stations) and mesh kept constant at all stages but the reference model was updated. Each stage consisted of five inversion iterations, wherein both the reference and starting models were set as the resulting model from the previous stage. For both the Hengill and Krafla inversions, five

Table 1
Inversion parameters and settings of the inversion codes used for the Hengill and Krafla MT datasets.

		WSINV3DMT	EMGeo	MT3DInv
<i>Hengill inversions</i>				
Data	Frequencies	10^2 – 10^{-3} , 5 per decade 26 in total	$10^{2.3}$ – 10^{-2} , 3 per decade 15 in total	10^2 – $10^{-2.3}$, 3 per decade 16 in total
Core mesh	Number stations Number of cells x - y - z Smallest cell [m]	144 39–47–18 $500 \times 500 \times 8$	138 79–93–50 $250 \times 250 \times 50$	132 79–94–67 $250 \times 250 \times 50$
Initial starting model [Ohm-m]		50	30	16
<i>Krafla inversions</i>				
Data	Frequencies	10^2 – 10^{-3} , 5 per decade 26 in total	$10^{2.3}$ – 10^{-2} , 3 per decade 15 in total	10^2 – $10^{-2.6}$, 5 per decade 24 in total
Core mesh	Number stations Number of cells x - y - z Smallest cell [m]	122 37–33–18 $300 \times 300 \times 8$	130 62–51–84 $250 \times 250 \times 50$	116 49–45–59 $250 \times 250 \times 50$
Initial starting model [Ohm-m]		20	30	20

stages were required for the procedure to converge and to recover a satisfactory model.

4.2. EMGeo

Some of the key parameters used in the implementation of the EMGeo inversion code for the Hengill and Krafla areas are given in [Table 1](#).

In both areas, the mesh is parallel to the UTM grid. The size of the padding cells that surrounded the core mesh progressively increases by a factor of 1.2 away from the core mesh, until the lateral model boundary is approximately five skin depths away from the core mesh. A vertical cell thickness of 50 m is used in the topographic range; this thickness was continuously increased to 500 m and then kept constant to 10 km depth. Below that depth, the cell thickness grows by a factor of 1.2. The model extends 100 km above and below sea level, with approximately 20 cells above topography, which were included in the model domain. For both areas, the inversion is constructed with the same inversion input parameters. EMGeo employs a Laplacian smoothness model regularization and a cooling scheme for the trade-off parameter, as described previously. A global bound is used, forcing the resistivity values to be between 2000 and 1 Ohm-m. The data misfit used is 5% of the given data value. In order to properly fit the full bandwidth of data, the inversion procedure is sequenced into two stages as described in detail by [Lindsey and Newman \(2015\)](#). In the first stage, only frequencies below 1 Hz were inverted on a coarse mesh (smallest core cell size of 500 m × 500 m × 50 m). After fitting the low frequency data, the resulting coarse model was re-parameterized onto a fine mesh (smallest core cells size of 250 m × 250 m × 50 m), which was sequentially used as a starting model for the second stage. In the second stage, the data from the full frequency range were used.

4.3. MT3Dinv

Some of the key parameters used in the implementation of MT3Dinv inversion code for the Hengill and Krafla areas are given in [Table 1](#).

In both areas, the mesh is parallel to the UTM grid. Horizontally, the padding cells around the core mesh are progressively increased by a factor of 1.4 away for the core mesh. Within the core mesh, the cell thickness was incrementally increased with depth from 50 m to 650 m at 10 km depth, beyond which the thickness grew by a factor of 1.4. In the topographic region, a vertical thickness of 50 m was used to discretize the topographic relief in the areas. The inversions were set up in similar ways for both areas. Global bounds were used to force all the values of the cells in the model to be between 5000 and 0.1 Ohm-m, the model regularization parameters $\alpha_{x,y,z}$ were set to 1, and α_s was set to 10^{-7} , much smaller relative to $\alpha_{x,y,z}$, in order to force smoothness in the recovered model. The data uncertainties used for the inversion were set as 10% of the data value, plus an error floor set to be 5% of the mean for the off-diagonal elements at each frequency.

To increase the efficiency of the inversion procedure, it was conducted in stages, with the mesh resolution coupled with the subsample of the frequencies used in the data analysis. For the Hengill inversion, the procedure was conducted in three stages, as described in [Rosenkjaer and Oldenburg \(2012\)](#). The workflow for the Krafla data set contained only two stages. In the first stage, a coarse mesh (core cell size of 500 m × 500 m × 75 m) was used to invert 12 frequencies below 10 Hz. The resulting model was re-parameterized onto a finer mesh (core cell size of cell size 250 m × 250 m × 50 m) and the full frequency range in [Table 1](#) was used. During inversion using the coarse mesh, the reference model was not updated at the start of each new β step; however, during

the inversion with the fine mesh, the reference model was updated at that point.

5. Comparison of resistivity models

Here we describe a novel set of metrics to evaluate structural features in 3D MT resistivity models and then use these metrics to interrogate the retrieved models for Krafla and Hengill. We propose using gradient and Laplacian operators, along with resistivity models, to add a quantitative analysis to the comparison of the recovered models. We further propose to use a cross-gradient comparison between two models to map out the structural correlation between the respective models. The goal of comparing inversion results in this way is to identify robust resistivity structures that are required by the data and that are therefore better suited for geological and petrological interpretation. All model analyses and visualization were done with Python scripts, using a combination of Numpy ([Oliphant, 2007](#)) and Visualization Toolkit (VTK) ([Schroeder et al., 2006](#)). Our ultimate goal is to assess and identify common features in the models. These common features are discussed and interpreted in terms of geology in [Gasperikova et al. \(2015\)](#).

5.1. Description of comparison procedure

All the inversions were run on different meshes, so in order to conduct comparisons, we had to transfer all the models to a common grid. For the comparison grid, we used only the areas in the models covered by data with topography incorporated. Calculations of gradient and Laplacian parameters were performed on the original meshes, and then transformed to the comparison grid with an inverse-distance weighted interpolation scheme. Because inversions using WSINV3DMT did not include topography, we needed an additional processing step during the regridding process for the WSINV3DMT models, to shift cells in the vertical direction.

5.1.1. Definitions of the parameters

We propose to extract structural information from 3D MT models that is especially useful when comparing two models. The approach uses a series of metrics based on the gradient, cross-gradient and Laplacian operators. In the derived calculations below, we use $m = \log_{10}(\text{model resistivity})$.

The model gradient is calculated as

$$\nabla m = \left[\frac{\partial m}{\partial x} \hat{i}, \quad \frac{\partial m}{\partial y} \hat{j}, \quad \frac{\partial m}{\partial z} \hat{k} \right], \quad (8)$$

where the gradient vector maps the change in resistivity of adjacent cells scaled by the distance between their cell centers in the three orthogonal directions. The gradient calculations of the models use a cell-centered discretization implemented in VTK. For visualization of the gradient, we use the magnitude of the gradient,

$$|\nabla m| = \sqrt{\left(\frac{\partial m}{\partial x} \right)^2 + \left(\frac{\partial m}{\partial y} \right)^2 + \left(\frac{\partial m}{\partial z} \right)^2} \quad (9)$$

where the gradient magnitude is a scalar of the square root of the sum of the squared three orthogonal gradient components. It maps the magnitude of the change in resistivity, irrespective of the resistivity increasing or decreasing.

The Laplacian is calculated as

$$\nabla^2 m = \left(\frac{\partial^2 m}{\partial x^2} + \frac{\partial^2 m}{\partial y^2} + \frac{\partial^2 m}{\partial z^2} \right), \quad (10)$$

The Laplacian gives an estimate of the curvature of the resistivity in all directions, with a positive value correlating with a positive (upward) curvature, and similarly a negative value correlating with

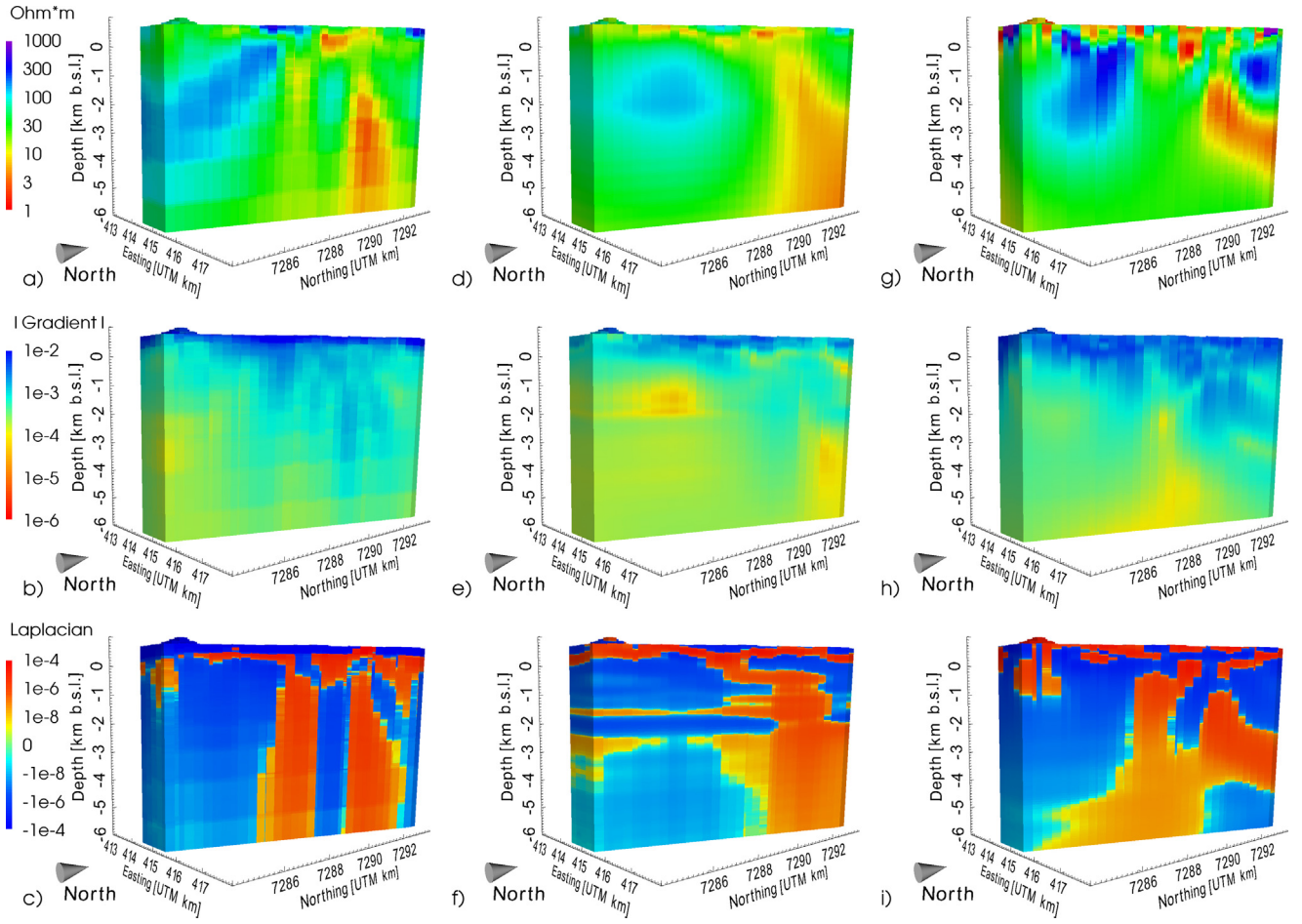


Fig. 5. A cross section along the main fissure in Krafla: (a), resistivity, (b) gradient, and (c) Laplacian are for results obtained with WSINV3DMT; (d) resistivity, (e) gradient, and (f) Laplacian are for results obtained with EMGeo; and (g) resistivity, (h) gradient, and (i) Laplacian are for results obtained with MT3DInv.

a negative (downward) curvature in the model. Related to the resistivity structure, a positive Laplacian correlates to features in which the resistivity increases at a faster rate compared to its surroundings, and a negative Laplacian corresponds to features in which the resistivity decreases at a faster rate compared to its surroundings.

To compare two resistivity models (m_1 and m_2) directly, we use the cross-gradient (cross products of gradients) between the two models

$$\nabla m_1 \times \nabla m_2 = \left[\left(\frac{\partial m_1}{\partial y} \frac{\partial m_2}{\partial z} - \frac{\partial m_1}{\partial z} \frac{\partial m_2}{\partial y} \right) \hat{i} + \left(\frac{\partial m_1}{\partial x} \frac{\partial m_2}{\partial z} - \frac{\partial m_1}{\partial z} \frac{\partial m_2}{\partial x} \right) \hat{j} + \left(\frac{\partial m_1}{\partial x} \frac{\partial m_2}{\partial y} - \frac{\partial m_1}{\partial y} \frac{\partial m_2}{\partial x} \right) \hat{k} \right], \quad (11)$$

where the cross-gradient is a vector mapping the differences of the gradients of the two models.

Since the result of Eq. (11) is a vector, for ease of viewing and illustration, we use its normalized magnitude,

$$\text{Norm}(\nabla m_1 \times \nabla m_2) = \frac{|\nabla m_1 \times \nabla m_2|}{|\nabla m_1| |\nabla m_2|}. \quad (12)$$

We implemented a minimum threshold on $|\nabla m_1|$ and $|\nabla m_2|$ to avoid the problem of dividing by a number close to 0. This problem occurs where there is little or no structure present in one or both models. The threshold was set to be 1.5 standard devia-

tions from the mean of the magnitude. Values that fall below this threshold are not considered (i.e., value set to NaN “not a number”), which forces the result for these cells from Eq. (12) to be NaN, as well as illustrating that the normalization is ill-posed. The aim of using the parameters discussed above is to highlight structures recovered in the resistivity models and help with a structural comparison between the models. Illustration of the quantitative power of these metrics is discussed using idealized synthetic examples in Appendix A.

5.2. Krafla

Cross-sections along the profile shown as black lines in Fig. 1 resulting from the inversion codes described in Sections 3.1–3.3 are shown in Fig. 5a, d, and g, respectively. Corresponding gradient magnitudes of each resistivity model are shown in Fig. 5b, e, and h, and the Laplacians of these models are shown in Fig. 5c, f, and i.

In the near surface, the WSINV3DMT model in Fig. 5a is resistive (>200 Ohm·m), but there is a discontinuous conductive region beneath (ranging from 10 to 25 Ohm·m), which connects upward to the surface in places. A resistive body (100–500 Ohm·m) is seen in the southern part of the model (centered at 7286 N, depth of 2 km), but two conductive vertical structures (both less than 10 Ohm·m) are observed in the central (7289 N) and northern (7291 N) part of the section. The northern conductive structure is more conductive, larger and discernible. In Fig. 5b, the magnitude of the gradient is highest in the near surface, and the vertical contacts are seen as high amplitude vertical stripes. The Laplacian in panel (c) reveals

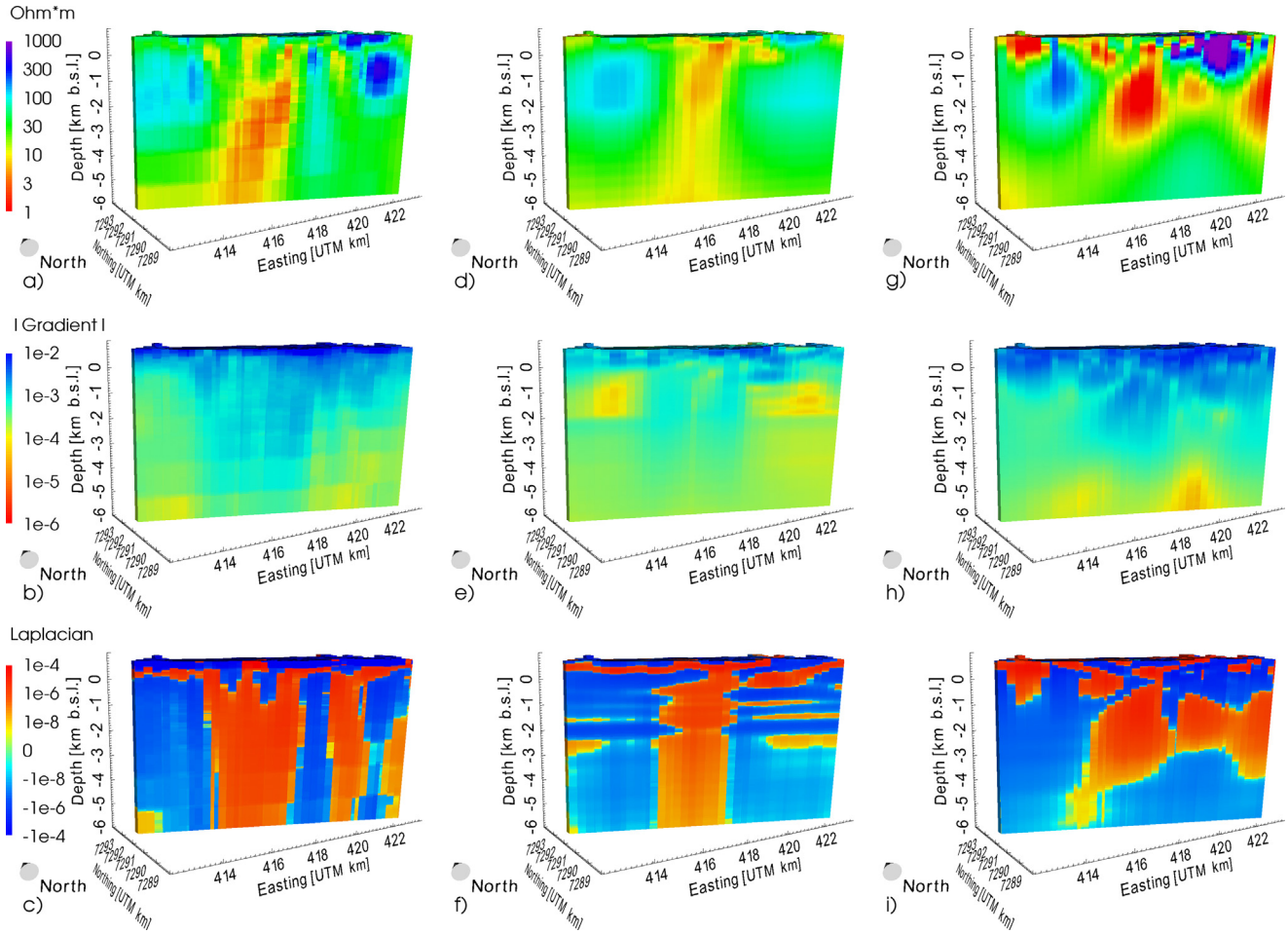


Fig. 6. A cross section across the main fissure in Krafla (line B in Fig. 1): (a), resistivity, (b) gradient, and (c) Laplacian are for results obtained with WSINV3DMT; (d) resistivity, (e) gradient, and (f) Laplacian are for results obtained with EMGeo; and (g) resistivity, (h) gradient, and (i) Laplacian are for results obtained with MT3DInv.

two distinct conductive bodies as upward curved pillars with a clear permutation of the curvature at the locations of the conductive structures in panel (a).

The surface resistivity of the EMGeo model in Fig. 5d is conductive above the resistive core in the southern part of the section (7285 N), connecting to a fairly continuous layer with resistivity less than 10 Ohm-m, though there are narrow gaps of relatively higher resistivity. A conductive zone (<15 Ohm-m) is present in the northern part (centered around 7291 N) of the section. This conductive zone comes within 1 km of the surface and has a large base at depth. The model gradient and Laplacian in panels (e) and (f) illustrate the dominant resistive structure to the south and the conductive zone to the north. In panel (f), horizontal features are revealed that are not apparent in the resistivity model in panel (d). We have determined that these are artifacts resulting from the reparameterization of the model (coarse grid to fine grid), as discussed in Section 4.2.

The MT3DInv resistivity model in Fig. 5g shows a resemblance to the model in panel (a); however, the model in panel (g) has fewer vertical structures, and the conductive overburden is more scattered. There is a dominant resistivity structure in the south and a conductive zone in the north (centered in similar locations as in panels (a) and (d)), extending from a depth of 5 km to the near surface. In the center of the section (at 7290 N), low-amplitude fluctuations are detected, which are seen as a zone of low gradient in panel (h). The model Laplacian in panel (i) illustrates the resistive body in the south and the conductive zone in

the north as downward and upward curvature features, respectively.

Fig. 6 shows a different cross-sectional view of the Krafla resistivity models; the view in Fig. 6 is perpendicular to the view in Fig. 5 (see Fig. 1 for exact orientation of these views). The vertical conductive structures seen at 7291 N in all three models in Fig. 5a, d and g are clearly identifiable in all the resistivity sections in Fig. 6a, d and g centered at 417 E. All the structures are similar in width (2 km), but in the MT3DInv model in panel (g), the resistivity is lower (~2 Ohm-m) and stops at 3.5 km depth. It is also evident that the resistive bodies in the eastern part of the sections (422 E) vary considerably. The resistive body in panel (a) is lower in amplitude (100–200 Ohm-m) and has a larger footprint (about 3 km wide) compared to panel (d), where the body's width is 1.5 km between the 100 Ohm-m surface and the peak amplitude of close to 800 Ohm-m. The resistive body in panel (g) is highly resistive (>1000 Ohm-m) and forms a continuous feature from the surface to a depth of about 1 km. The conductive body (<10 Ohm-m) on the eastern most end of the section (423 E) in panel (g) is not seen in the other models; furthermore, this feature lies at the edge of the data coverage. Therefore, it is likely that this model feature is an artifact of the inversion procedure.

The gradients of the models in panels (b), (e) and (h), show that the changes are occurring at a high rate (amplitude >1 e⁻⁴) in the near surface and at moderate depth in the central part of the section, but below 4 km depth and closer to the edges of the models, gradient magnitude is close to or below 1 e⁻⁴. As in Fig. 5, the Laplacian of

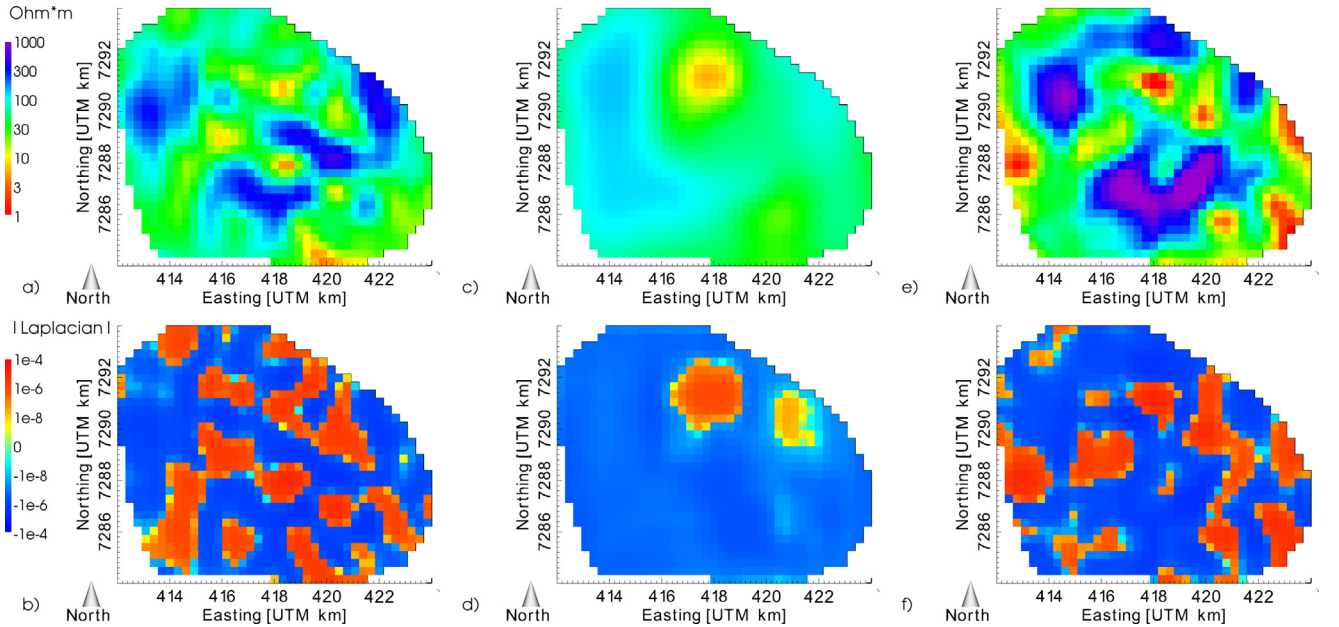


Fig. 7. Depth slices through the Krafla models at depth of 1000 m.b.s.l. Panels (a) and (b) show resistivity and Laplacian, respectively, for the results obtained with WSINV3DMT; (c) and (d) show results obtained with EMGeo; and (e) and (f) show results obtained with MT3Dinv.

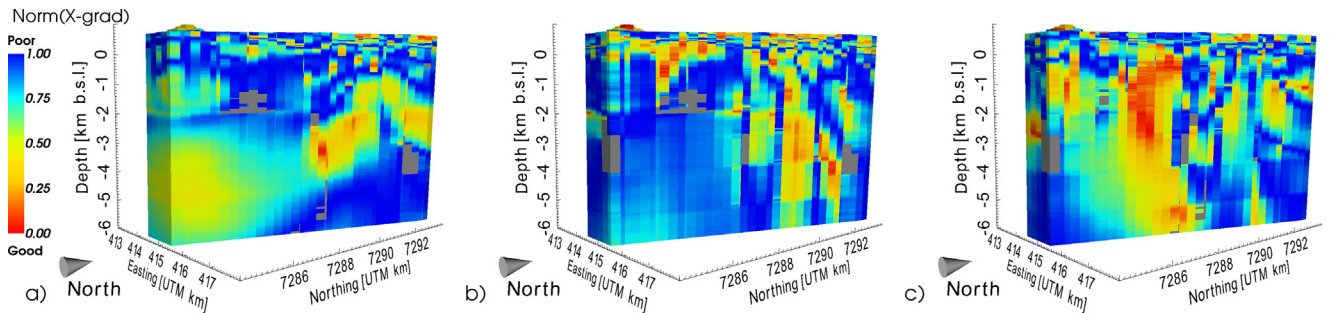


Fig. 8. Normalized cross-gradient sections (section A in Fig. 1) for the Krafla resistivity models: (a) EMGeo and MT3Dinv, (b) WSINV3DMT and EMGeo, and (c) WSINV3DMT and MT3Dinv, respectively. The grayed out area are zones where the gradient falls below threshold and cannot be reliably employed as described in Section 5.1. Values below 0.5 indicate good correlation between the respective models.

the sections in Fig. 6 illustrates the relative structural coincidence of the vertical conductive bodies recovered in all the models.

The vertical conductive structure reaching the near surface and the resistive core in the southwest seen in the panels of Figs. 5 and 6 for all three models, increase confidence in the geological importance of these structures. As well, all models have a conductive zone below a surface resistor, but the shape and magnitudes of this conductor vary considerably between the models. Comparison of the models at a depth of 1000 m.b.s.l. (Fig. 7) reveals SW-NE and NW-SE striking lineaments of structures in both the recovered models in panels (a) and (e). However, no such features are noticeable in the recovered model in panel (c). Possible explanations for these structural differences in the models are the variations in model regularization and its weight in the objective function of the inversion codes.

In both panels (a) and (e) of Fig. 7, the resistive structures in the northwest (414 E, 7290 N) and south (418 E, 7288 N) are noticeable. The resistive features are broken up by linearly trending conductive structures, striking SW-NE and NW-SE. The southeast resistive structure in panel (e) is seen as a single body with an isolated increased conductive feature in the center, compared to a linear break in the same structure in panel (a). This is further seen in

panels (b) and (f) in the Laplacian of the models, where the linear aligned structures are emphasized. However, the match is not complete: there are corresponding structures in both models, but the size and shape differ considerably.

In comparing the model in Fig. 7, panel (c), to the others in panels (a) and (e), we do not find correspondence in the smaller scale structures. The structure in panel (c) has less detail: it shows a large conductive feature in the northwest and a smaller feature in the southeast in an otherwise fairly resistive background (higher than 80 Ohm·m). The locations of these features correspond to structures of the same dominant resistivity in panels (a) and (e), but the structures in panel (c) have less detail. This is seen in panel (d), where only the conductive feature in the north is rendered using curvature.

Fig. 8 shows results using the cross-product comparisons described in Section 5.1 (section A in Fig. 1) where the normalized cross-gradient from EMGEO and MT3Dinv, WSINV3DMT and EMGEO, and WSINV3DMT and MT3Dinv models are illustrated in panels (a), (b), and (c), respectively.

The cross-gradients shown in Fig. 8 highlight the structural variation present in the models. More structural correlation is found in the cross-gradients in panel (c), especially in the center of the

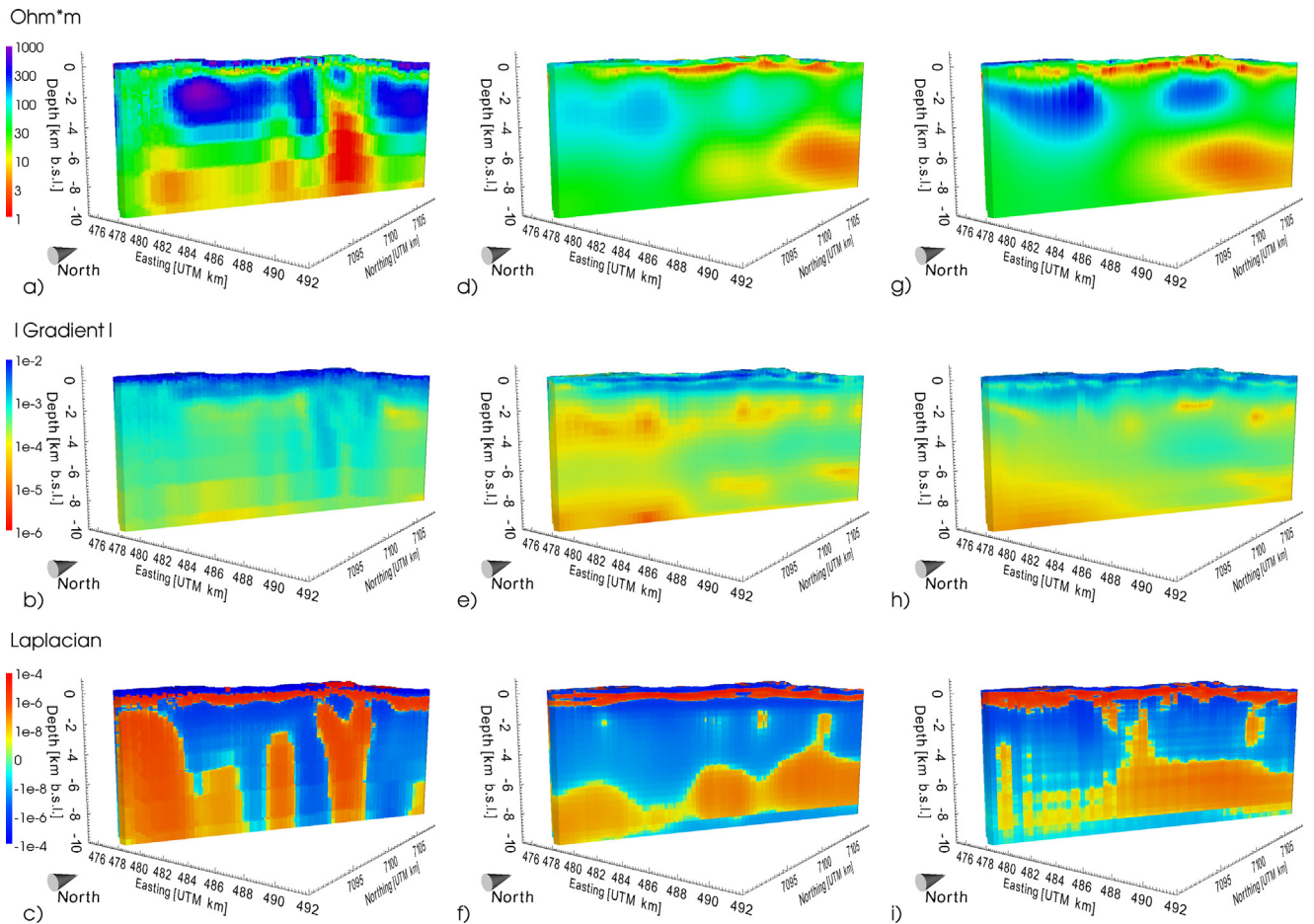


Fig. 9. Cross-section along the main fissure swarm (line A in Fig. 3) in Hengill showing (a) resistivity, (b) gradient, and (c) Laplacian for results obtained with WSIINV3DMT; (d) resistivity, (e) gradient, and (f) Laplacian for results obtained with EMGeo; and (g) resistivity, (h) gradient, and (i) Laplacian, for results obtained with MT3Dinv.

section associated with contact of the resistive body in the south. However, there appears to be less structural correlation in other regions, especially at depth.

5.3. Hengill

The resulting inversion models using the inversion codes described in Sections 3.1–3.3 are shown in Figs. 9 and 10 as cross-sections along and across the fissure directions in the area, respectively (black lines A and B in Fig. 3). All the models show the characteristic structure of a high-temperature geothermal system: a resistive surface underlain by a conductive zone, which resides over a resistive core region; and a deep conductor to the north. Also shown are structural maps (gradient and Laplacian) for the models, where similarity in the maps indicate structural correlations between respective models.

The surface of the WSIINV3DMT model in Fig. 9a is resistive (~500 Ohm·m), with that surface underlain by a thin conductive layer (~10 Ohm·m). The resistive core is fairly uniform in thickness, with resistivity between 500 and 1000 Ohm·m, but is broken by a moderately conductive zone (~50 Ohm·m) in the southern end (7090 N) and a highly conductive zone (<5 Ohm·m) in the northern part of the section. There is considerable contrast in the resistivity between the conductive breaks and resistive core (three orders of magnitude), which is emphasized by the high-magnitude values of the gradient ($>1 \text{ e}^{-3}$) in panel (b). Fig. 9c shows the Laplacian of the model, where the breaks in the resistive core are seen as pillars with positive curvature.

The thickness of the conductive overburden in the EMGeo model shown in Fig. 9d is noticeably greater than in panel (a). However, the resistive core in (d) is lower in amplitude (~150 Ohm·m), and the deeper conductor is mainly observed in the northern part of the model. Vertical conductive breaks (~60 Ohm·m) in the resistive core are observed in the center (482 E, 7102 N) and the northern part (484 E, 7105 N) of the section. In panel (e), a relatively thick layer (1–2 km thick) of low gradient (less than 5 e^{-5}) is mapped in the zone of the resistive core, indicating a constant resistivity in the core. No clear changes in the gradient are observed associated with the two conductive breaks in the resistive core, but the Laplacian in panel (f) reveals a positive curvature in the northern more of the conductive breaks.

The MT3Dinv resistivity model in Fig. 9g shows very similar structures to the model in panel (d). For example, a moderately resistive surface (~200 Ohm·m) is recovered, underlain by a fairly continuous conductive layer that varies in thickness, as in the model in panel (d). The resistive core is more resistive in panel (d) (~500 Ohm·m), with similar vertical conductive breaks and at the same locations as in panel (d). The resistive core has a thin, low gradient layer ($<5 \text{ e}^{-5}$) and moderate lateral increase ($\sim 2 \text{ e}^{-4}$), which coincides with the resistivity breaks in panel (g). Both of these breaks have a positive curvature in the Laplacian in panel (i).

Fig. 10 shows a different cross-sectional view of the Hengill resistivity models; the view is close to perpendicular to the view in Fig. 9 (see Fig. 3 for exact orientation of these views). As in

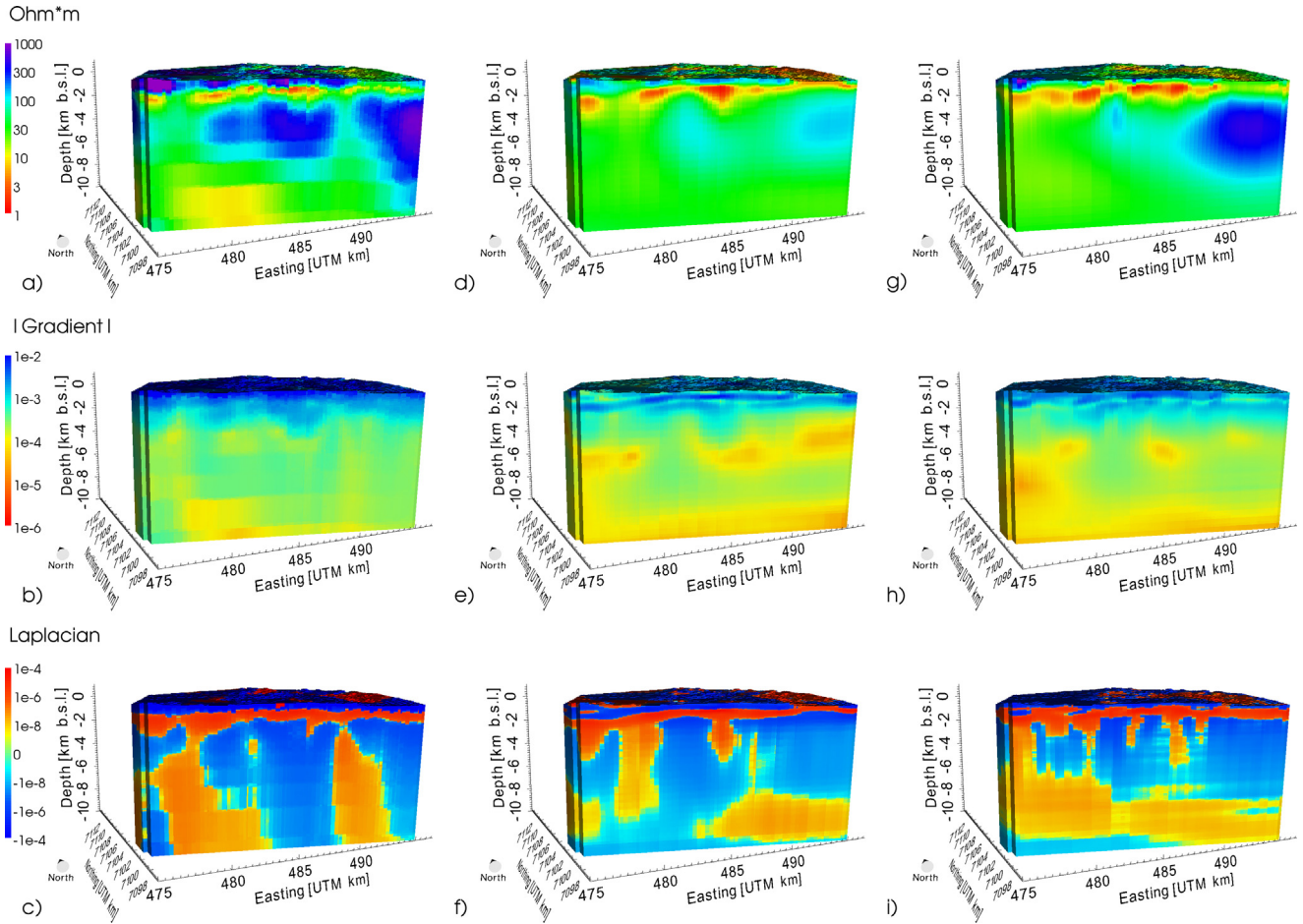


Fig. 10. Cross-section across the main fissure swarm (line B in Fig. 3) in Hengill showing (a) resistivity, (b) gradient, and (c) Laplacian for results obtained with WSINV3DMT; (d) resistivity, (e) gradient, and (f) Laplacian for results obtained with EMGeo; and (g) resistivity, (h) gradient, and (i) Laplacian, for results obtained with MT3DInv.

Fig. 9, the resistivity sections in panels (d) and (g) show considerable resemblance. A resistive body is seen at the eastern end (490 E) in both sections, but a contrast in resistivity is observable, where the model in panel (g) has a maximum of 600 Ohm-m compared to 200 Ohm-m in panel (d). Lower magnitude resistive body in the central part (485 E) is seen in both panels, overlain by a noticeable thicker conductive layer. The model in panel (a) shares the character of the other models in panels (d) and (g), but the near-surface conductive layer appears to be more resistive (5 Ohm-m compared to 2 Ohm-m in models in panels (d) and (g)) and the amplitude of the resistive bodies are considerable greater. Examining the gradient in panels (e) and (h), reveals the near-surface conductive layer to be a high magnitude gradient contrast, followed by the lows associated with the resistive bodies. The gradient in panel (a) stands out as before, uncovering vertical features around 490 E, which are supported by the Laplacian in panel (c), as contrasting upward and downward curved features.

By comparing the models and the structural derivatives in Figs. 9 and 10, one sees that the similarities between the resistivity models in panels (d) and (g) are greater than for the model in panel (a). However, all models agree on the main structures, recovering a resistive surface layer with decreased resistivity coinciding with mapped surface alterations; a shallow conductive layer that varies in depth and in thickness over the area; and a resistive core region that is broken up by moderately conductive zones. The main differences in the WSINV3DMT model in panel (a) compared with the other two models are the pronounced verti-

cal structures, especially below 4 km depth. It is also noticeable that the cell resolution in the WSINV3DMT model is relatively poorer at depth, due to the low number of vertical cells in the mesh.

Horizontal maps at a depth of 4000 m.b.s.l. are shown in Fig. 11, where modeled resistivity and Laplacian values are shown in panels (a) and (b), (c) and (d), and (e) and (f) for recovered models from codes described in Sections 3.1–3.3, respectively. The structural correspondence of the models in (c) and (e) is clear, with the southeast part of the sections predominantly resistive (resistivity greater than 80 Ohm-m) and the northwestern part more conductive. In panel (a), there are more permutations in the structure, with lineaments of structures with a northwest-southeasterly strike present.

Fig. 12a–c show the cross-gradient results from EMGEO and MT3DInv, WSINV3DMT and EMGEO, and WSINV3DMT and MT3DInv, respectively.

The normalized cross-gradient presented in Fig. 12a confirms the similarities of the models shown in Fig. 9b and c. Most of the values in Fig. 12a fall below 0.5, indicating a strong structural resemblance between the two models, confirming the observed similarities in the resistivity models in Figs. 9 and 10. The main discrepancies are seen in the near surface and at mid-depth in the resistive core region, where structural boundaries do not correlate well. Panels (b) and (c) show the inconsistent interface at the top and bottom of near-surface conductive layers in the models, seen as a thin layer of poor correlation (value close to 1). Major discrepancies are seen at 486 E, 7105 N in the section, where a conductive

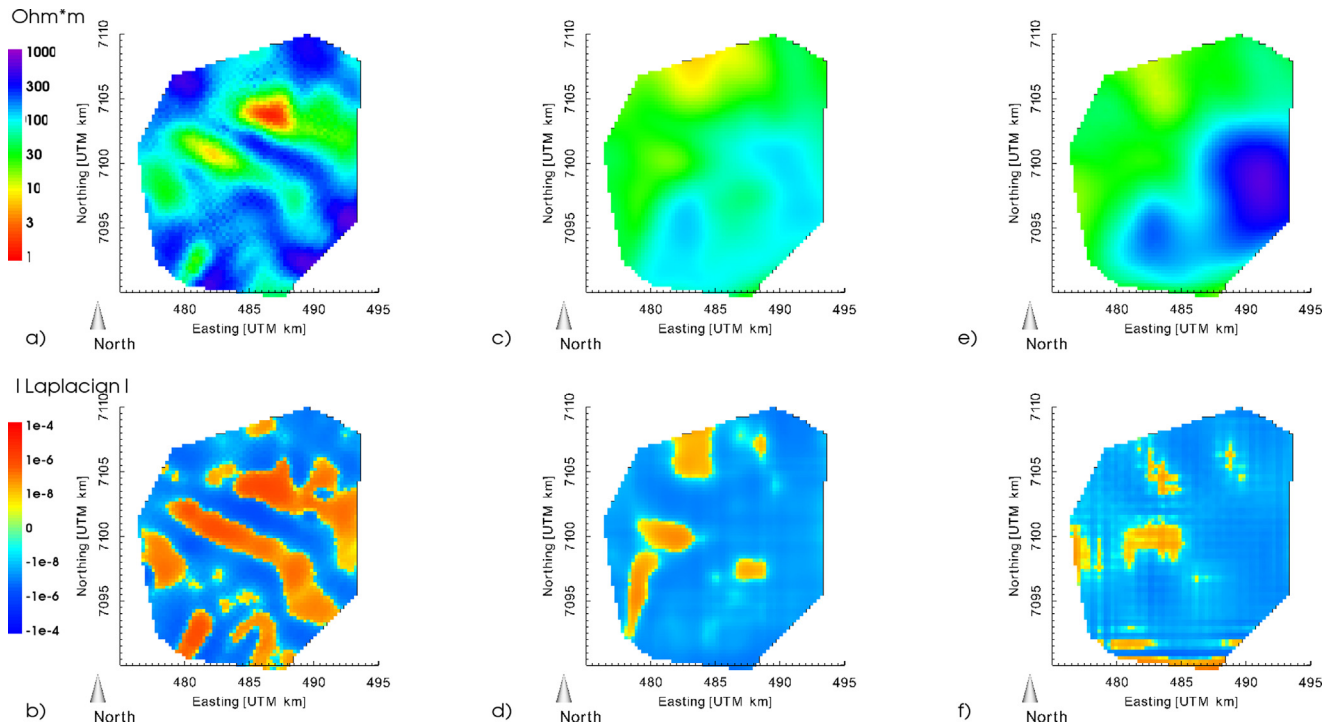


Fig. 11. Depth slices through the Hengill models at depth of 4000 m.b.s.l. Panels (a) and (b) show the resistivity model and Laplacian parameter, respectively, for results obtained with WSINV3DMT; (c) and (d) show corresponding results for EMGeo; and (e) and (f) show results obtained with MT3DInv.

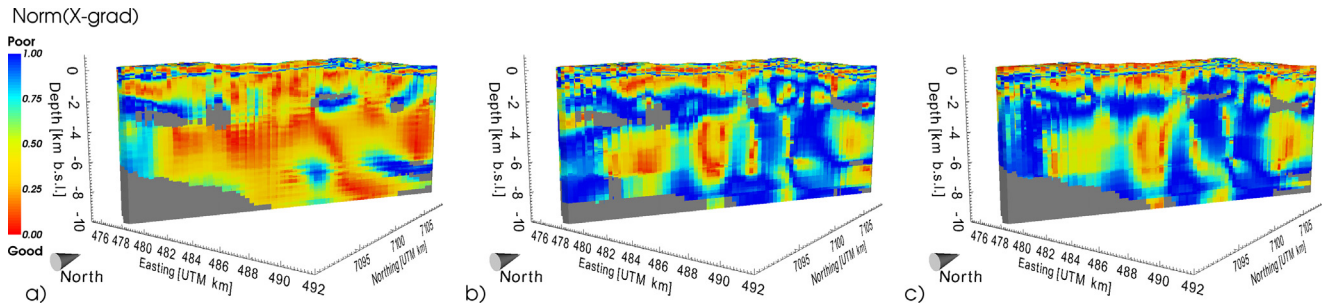


Fig. 12. Normalized cross-gradient sections (line A in Fig. 3) for resulting resistivity models at Hengill between (a) EMGeo and MT3DInv codes, (b) WSINV3DMT and EMGeo codes, and (c) WSINV3DMT and MT3DInv codes, respectively. The grayed-out areas are zones where the gradient falls below threshold and cannot be reliably employed, as described in Section 5.1. Values below 0.5 indicate good correlation between the respective models.

body is seen in the model in Fig. 9a that is not recovered in the models in (d) and (g).

6. Conclusions

In this paper, we present a comparison of three 3D MT inversion codes using field data from the Krafla and Hengill geothermal fields in Iceland. The goal was to assess the robustness of the inversion procedure in a real data scenario, where results are known to strongly depend on the quality of data, assignment of data uncertainties, model discretization, and other potential sources of bias introduced during the inversion workflow. In general, the non-uniqueness of the 3D MT inverse problem allows data to be fit to a similar level with different structures; confidence in a particular model feature is thus derived from different modeling algorithms and settings retrieving similar and coincident structures. The three inversion codes were run independently, and it was up to the modeler to set up his/her inversion in an optimal way; the only

restriction was that all modelers had to use the same initial data sets.

Recovered resistivity values can be misleading where the dynamic range of recovered models can be significantly different. Moreover, the differences between two models are not always obvious, which can obscure interpretation. We show computing the model gradients, Laplacian, and normalized cross-gradient can be useful, specifically when characterizing subtle structural features and for comparing two different models. These quantitative metrics are found to enhance model appraisal and geological interpretation.

Different model results from Krafla are fairly inconsistent; however, all three codes recover:

- (1) A fairly resistive surface, underlain by a conductive layer
- (2) A deep conductive (<10 Ohm·m) zone to the north/northwest
- (3) Resistive bodies in the south/southeast and northwestern parts of the survey area at moderate depth.

Feature (2) rises from depths of 5 km. Two inversion codes (WSINV3DMT and MT3DInv) recover models with more structure relative to the third code (EMGeo); nevertheless, structural analysis reveals a fair degree of correspondence between all resistivity models. This structural consistency, adds a level of confidence to the overall model interpretations, despite individual model differences. One explanation for the large range of acceptable Krafla resistivity models is data quality. Poor data quality can require the inversion codes to introduce extraneous structure in an attempt to lower the data misfit.

The results from Hengill show more coincident resistivity structures relative to Krafla. All three models recovered resistivity structures corresponding to the characteristic resistivity structure of geothermal systems, with an up-doming around the central volcano. All models recover:

- (1) A conductive (<10 Ohm-m) near-surface layer (within 1.5 km from the surface)
- (2) A moderately deep resistive core (>100 Ohm-m) broken in places by moderately conductive zones

(3) A deep conductor in the northeastern part of Hengill.

The greater consistency of recovered models at Hengill compared with the results from Krafla increases confidence that these structures are required to fit the data, and are not artifacts from the inversion process. Both EMGeo and MT3DInv recover models that are structurally very similar, as seen in the resistivity models, highlighted in the structural derivatives of the recovered models, and further emphasized by cross-gradient analysis. The major difference between these two models and WSINV3DMT model can be seen at 486 E, 7105 N, where the WSINV3DMT recovers a vertical, relatively more conductive body compared to the moderately resistive zones in the other two codes. One plausible explanation for this difference is inversion design; the mesh used with WSINV3DMT expanded the thickness of cells much faster compared to EMGeo and MT3DInv; and in addition, both the grid and data were rotated by 30° E.

The structural similarities of the resistivity models discussed in this paper increase confidence that those structures are required by the data and arise from geological structures. [Gasperikova et al.](#)

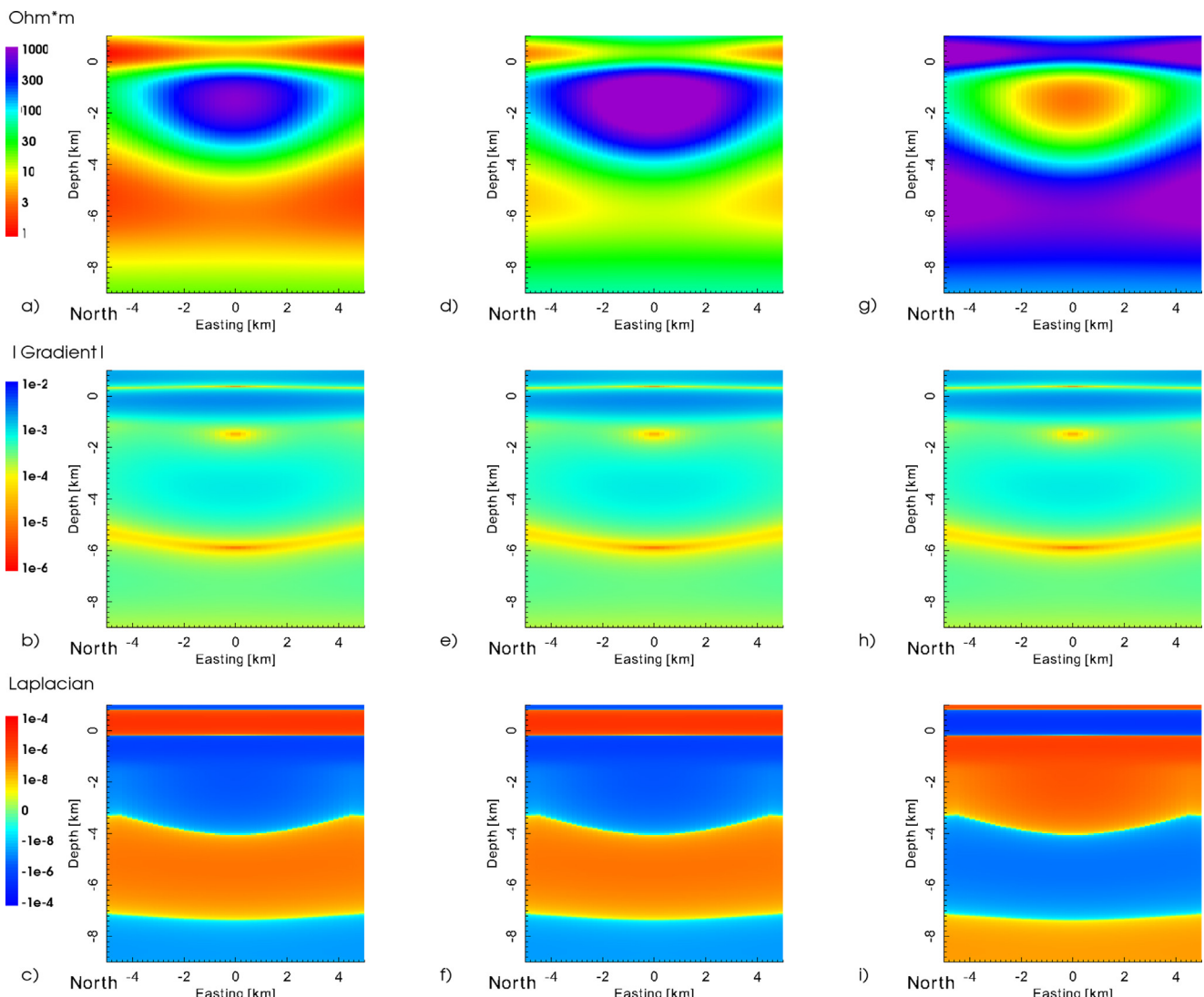


Fig. 13. Synthetic models with simple resistivity structures are shown in (a), (d), and (g), with the corresponding magnitude of the gradient and Laplacian shown in (b) and (c); (e) and (f); (h) and (i), respectively. Relative changes in the structural trends in all the models are the same, seen as identical gradients in for all the models (b), (e), and (h). Notice that when a conductive body replaces a resistive body (as in (g), contrasting with (a) and (d)), this change is reflected in the Laplacian measure but not in the magnitude of the gradient.

(2015) discuss these structures in greater detail, and in particular their relationship to the known geology of the Krafla and Hengill geothermal areas.

Acknowledgements

This work was carried out at University of British Columbia and Iceland Geosurvey, with funding provided by Geothermal Research Group GEORG; and at Lawrence Berkeley National Laboratory, with funding provided by the US Department of Energy Geothermal Program Office under contract GT-480010-19823-10, and Office of Basic Energy Sciences under Award No. DE-AC02-05CH11231. We also want thank three anonymous reviewers for the valuable comments and suggestions to improve the manuscript.

Appendix A.

In the section we discuss and give examples of the parameters defined in Section 5.1.1. Since this analysis uses log 10 of the resistivity values, a change from 1000 to 100 Ohm-m is equivalent to a change from 10 to 1 Ohm-m between adjacent cells. Thus, if the

distance between these cell centers were 100 m, the resulting gradient magnitude is 10^{-2} . The Laplacian is sensitive to the sign of the gradient, resulting in either a positive or negative value depending on whether resistivity is increasing or decreasing, respectively. One cannot determine whether resistivity is increasing or decreasing solely by the gradient.

An illustration of these parameters is shown in Fig. 13. Simple resistivity models are shown in the top row (panels a, d, g). All the models can be characterized as three structures added to a background resistivity value; only the background and the relative amplitudes of the embedded structures change (i.e., the structural geometry is unchanged). Model (a) has a relatively conductive background of 30 Ohm-m, while Models (d) and (g) have relatively resistive backgrounds of 100 Ohm-m. Despite this difference, the gradient of the models, shown in the middle row (panels b, e, h) are the same, demonstrating that the background resistivity value has no effect on the gradient. The structures in Models (a), and (d) were constructed by adding positive resistivity values to the background, while the structure in Model (g) was constructed by adding negative resistivity values to the background. The opposite amplitude of the structures is not detected in the magnitude of the gradient

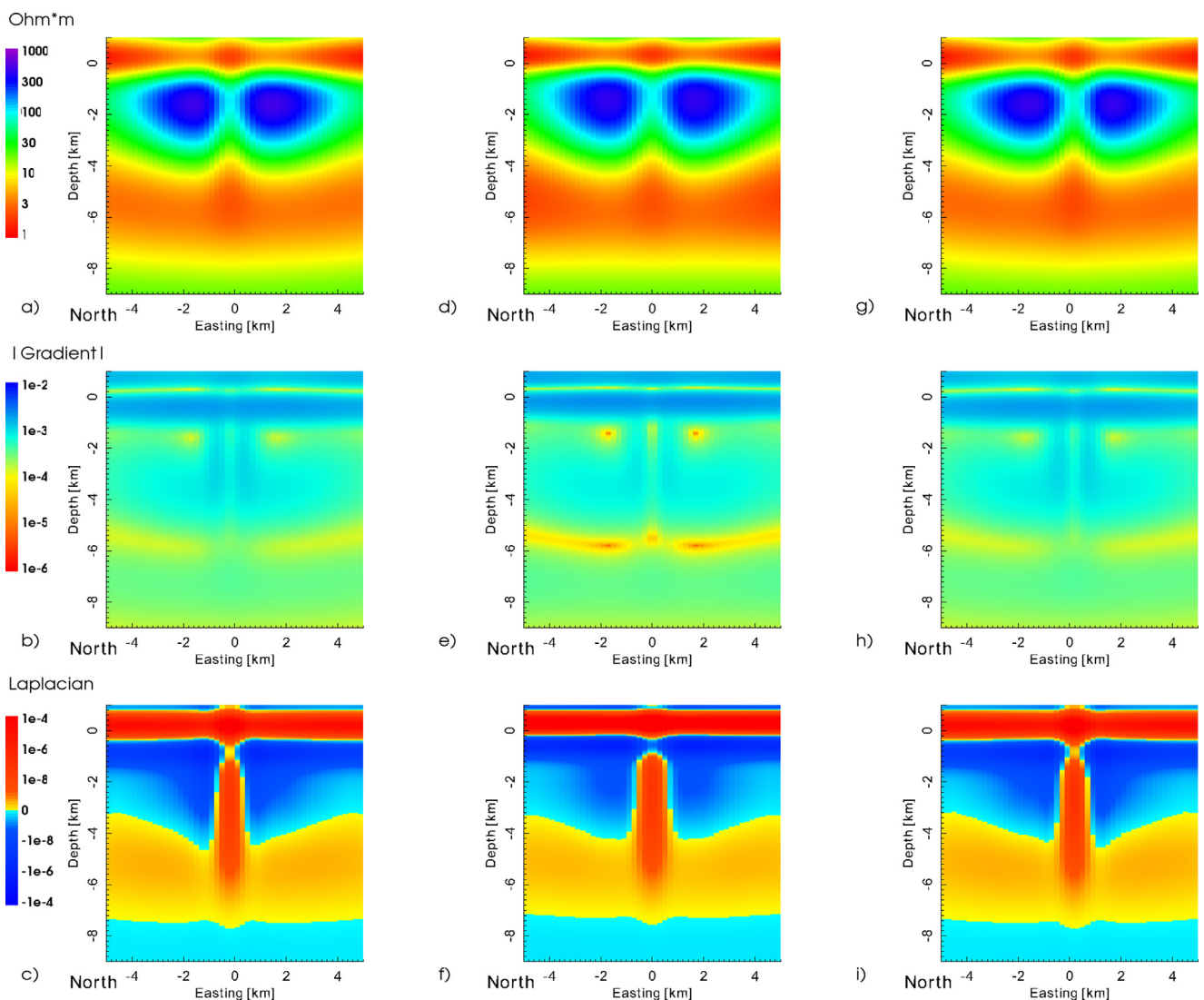


Fig. 14. Synthetic models with simple resistivity structures are shown in (a), (d), and (g), with the corresponding magnitude of the gradient and Laplacian shown in (b) and (c); (e) and (f); (h) and (i), respectively. The models all have the same background resistivity and same structures, but amplitude peaks are shifted in space, which are not easily detected without recourse to structural metrics, such as the gradient and Laplacian discussed in this paper.

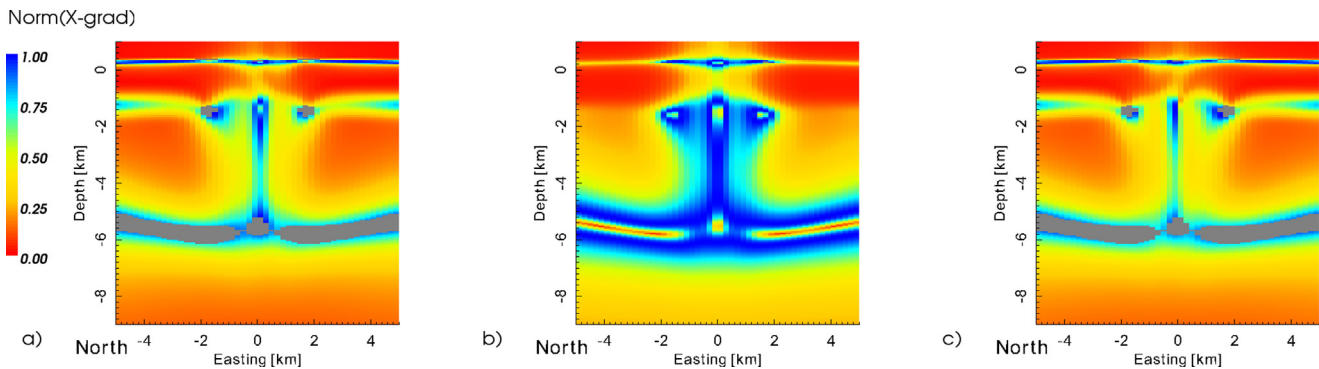


Fig. 15. Cross-gradients of resistivity models shown in Fig. 14: (a) the cross-gradient of models in Fig. 14 (d) and (g), (b) cross-gradient of models in Fig. 14 (a) and (g), and (c) cross-gradient of models in Fig. 14 (a) and (d). The gray regions in these plots are areas where either one of the gradients is very small, making the value of the cross-gradient NaN, and thus no color is plotted (see Section 5.1 for further details).

vector. However, the Laplacian of the models, shown in the bottom row (panels c, f, i), does show structural trends. For example, the Laplacians of model (a) and (d) shown in panels in (c) and (f), respectively, clearly show the models exhibiting similar structural trends, while the Laplacian of the model in (g) shown in panel (h), is clearly different. Since the gradients of all the models are the same, the cross-gradient is zero for all of them.

Fig. 14 shows cross-sectional views of three resistivity models that all have the same background resistivity of 30 Ohm-m. Each model is embedded with similar structures, a shallow conductive layer, a split resistive body, and a deep conductive layer. The structural dissimilarities of the models arise from spatial shifting of the amplitude peaks in the shallow and deep conductive layers and the break in the resistive body. All the amplitude peaks in Model (d) are centered, but in Models (a) and (g), the structures are shifted symmetrically about the center by 300 m, 800 m, and 2000 m laterally. The visual similarity of Models (a), (d), and (g) is clear. Panels (b), (e), and (h) show how these models have similar gradient magnitudes, but some differences can be seen. For example, in panel (e), the resistive structures and the deep conductive layer produce relatively large gradients where magnitudes below 1 e^{-5} are reached. Likewise, the Laplacian of Models (a), (d), and (g), shown in panels (c), (f), and (i), exemplify subtle differences. Nonetheless, the Laplacian for all the models shows a positive curvature associated with the break in the resistive layer.

Fig. 15 shows the cross-gradients of the resistivity models in Fig. 14a, d, and g. While the parameters shown in Fig. 14 reveal structural similarities between models, the cross-gradient parameter highlights model differences. The cross-gradients in panels (a) and (c) look similar, illustrating the symmetric spatial shifts of the structures shown in Fig. 14a and g, compared to the structure in (d). The grayed-out area in both figures corresponds to the low magnitude in the gradient in Fig. 14e, discussed above, which makes the cross-gradient difficult to determine (see Section 5.1 for further details). The cross-gradient in panel (b) exposes dissimilarities in gradient structures associated with the break in the resistive and the deep conductive layers. The magnitude of the normalized cross-gradient is high in these regions, indicating that the angle between the gradient vectors is approaching 90° .

The idealized modeling examples discussed above highlight advantages and disadvantages of the proposed metric parameters with respect to mapping structural coincidence in the models. Using different structural metrics together enables interpretation of subtle resistivity model features, and enhances comparison and model appraisal.

References

- Árnason, K., Eysteinsson, H., Hersir, G.P., 2010. Joint 1D inversion of TEM and MT data and 3D inversion of MT data in the Hengill area, SW Iceland. *Geothermics* 39, 13–34.
- Cagniard, L., 1953. Basic theory of the magneto-telluric method of geophysical prospecting. *Geophysics* 18, 605–635.
- Farquharson, C., Oldenburg, D., Haber, E., Shekhtman, R., 2002. An algorithm for the three-dimensional inversion of magnetotelluric data. In: 72nd SEG Annu. Meet., Salt Lake City, UT, pp. 649–652.
- Flóvenz, Ó.G., Hersir, G.P., Sæmundsson, K., Ármannsson, H., Friðriksson, T., 2012. Geothermal energy exploration techniques. In: Comprehensive Renewable Energy. Elsevier Ltd., pp. 51–94.
- Friðleifsson, G.Ó., Ármannsson, H., Guðmundsson, Á., Árnason, K., Mortensen, K.a., Pálsson, B., Einarrsson, G.M., 2014. Site selection for the well IDDP-1 at Krafla. *Geothermics* 49, 9–15.
- Gamble, T.D., Gouba, W.M., Clarke, J., 1979. Error analysis for remote reference magnetotellurics. *Geophysics* 44, 959–968.
- Gasperikova, E., Rosenkjaer, G.K., Arnason, K., Newman, G.A., Lindsey, N.J., 2015. Resistivity characterization of the Krafla and Hengill geothermal fields through 3D MT inverse modelling. *Geothermics* 57, 246–257.
- Heise, W., Caldwell, T.G., Bibby, H.M., Bannister, S.C., 2008. Three-dimensional modelling of magnetotelluric data from the Rotokawa geothermal field, Taupo Volcanic Zone, New Zealand. *Geophys. J. Int.* 173, 740–750.
- Hjartardóttir, Á.R., Einarsson, P., Bramham, E., Wright, T.J., 2012. The Krafla fissure swarm, Iceland, and its formation by rifting events. *Bull. Volcanol.* 74, 2139–2153.
- Kiyan, D., Jones, a.G., Vozar, J., 2013. The inability of magnetotelluric off-diagonal impedance tensor elements to sense oblique conductors in three-dimensional inversion. *Geophys. J. Int.* (18).
- Lindsey, N.J., Newman, G.a., 2015. Improved workflow for 3D inverse modeling of magnetotelluric data: examples from five geothermal systems. *Geothermics* 53, 527–532.
- Miensopust, M.P., Queralt, P., Jones, a.G., 2013. Magnetotelluric 3-D inversion – a review of two successful workshops on forward and inversion code testing and comparison. *Geophys. J. Int.* 193, 1216–1238.
- Newman, G., Alumbaugh, a.D.L., 2000. Three-dimensional magnetotelluric inversion using non-linear conjugate gradients. *Geophys. J. Int.* 140, 410–424.
- Newman, G.a., Boggs, P.T., 2004. Solution accelerators for large-scale three-dimensional electromagnetic inverse problems. *Inverse Probl.* 20, S151–S170.
- Newman, G., Gasperikova, a.E., Hoversten, G.M., Wannamaker, P.E., 2008. Three-dimensional magnetotelluric characterization of the Coso geothermal field. *Geothermics* 37, 369–399.
- Oldenburg, D., Li, Y., 2005. Inversion for applied geophysics: a tutorial. In: Butler, D.K. (Ed.), *Investigations in Geophysics*, 13. Society of Exploration Geophysicists, Tulsa, Oklahoma, pp. 89–150.
- Oiphant, T.E., 2007. Python for scientific computing. *Comput. Sci. Eng.*, 9.
- Rosenkjaer, G.K., 2011. Electromagnetic methods in geothermal exploration. 1D and 3D inversion of TEM and MT data from a synthetic geothermal area and the Hengill geothermal area, SW Iceland. University of Iceland.
- Rosenkjaer, G.K., Oldenburg, D.W., 2012. 3D inversion of MT data in geothermal exploration: a workflow and application to Hengill, Iceland. In: Thirty-Seventh Workshop on Geothermal Reservoir Engineering Stanford University, Stanford, California, January 30–February 1, 2012.
- Schroeder, W., Martin, K., Lorenzen, B., 2006. The Visualization Toolkit: An Object-Oriented Approach to 3D Graphics, 4th ed.

- Siripunvaraporn, W., 2011. Three-dimensional magnetotelluric inversion: an introductory guide for developers and users. *Surv. Geophys.* 33, 5–27.
- Siripunvaraporn, W., Egbert, G., 2009. WSINV3DMT: vertical magnetic field transfer function inversion and parallel implementation. *Phys. Earth Planet. Inter.* 173, 317–329.
- Siripunvaraporn, W., Egbert, G., Lenbury, Y., Uyeshima, M., 2005. Three-dimensional magnetotelluric inversion: data-space method. *Phys. Earth Planet. Inter.* 150, 3–14.
- Stark, M.A., Soyer, W., Hallinan, S., Watts, M.D., 2013. Distortion effects on magnetotelluric sounding data investigated by 3D modeling of high-resolution topography. *GRC Trans.*, 37.
- Vozoff, K., 1991. The magnetotelluric method. In: Naibighian, M. (Ed.), *Electromagnetic Methods in Applied Geophysics*. Society of Exploration Geophysicists, Tulsa, Oklahoma, pp. 641–711.